

# **Hot Electron Thermal Emission Spectroscopy**

Leon Oleschko  
Supervised by Peter Baum  
24.07.2025  
Universität Konstanz

# 1 Introduction

Ultrafast laser-matter interactions on femtosecond timescales create non-equilibrium electronic states that are fundamentally important for understanding energy dissipation in condensed matter systems. When intense femtosecond laser pulses interact with materials, they can generate populations of hot electrons with temperatures significantly exceeding the lattice temperature [1]. These transient hot electron populations have lifetimes on the order of hundreds of femtoseconds [2] and represent a critical intermediate state in ultrafast energy transfer processes. Hot carrier dynamics have attracted considerable interest for applications in next-generation photovoltaics, ultrafast terahertz photodetectors, and photocatalytic hydrogen production [3, 4].

The process of heating a bulk material by means of femtosecond laser pulses can be described with a two-temperature model [5]. In this framework, an external energy input first excites out-of-equilibrium electrons in the electron gas to a temperature  $T_e$ , while the lattice remains at an initial temperature  $T_l$ . For the short timescales relevant to hot electron dynamics, the lattice temperature can be assumed constant at room temperature, as thermal diffusion in the lattice occurs on much longer timescales than electron thermalization. Under this approximation, the temporal evolution of the electron temperature is governed by:

$$C_e(T_e) \frac{\partial T_e}{\partial t} = -G(T_e - T_l) + S(r, t), \quad (1)$$

where  $C_e(T_e)$  is the temperature-dependent electronic heat capacity,  $G$  is the electron-phonon coupling constant,  $T_l$  is the constant lattice temperature, and  $S(r, t)$  represents the laser source term. Since the electronic heat capacity  $C_e$  is much lower than the lattice heat capacity, the hot electron temperature can far exceed the lattice temperature during the initial femtoseconds following laser excitation [6]. The cooling dynamics involve complex mechanisms including strongly coupled optical phonons [7] and phonon-mediated relaxation processes [2]. Integration of this equation using realistic laser source terms (250 fs FWHM pulses at 1030 nm) predicts short-lived electronic temperatures upwards of 5650 K in graphite [5], far exceeding the constant lattice temperature during the sub-picosecond timescales of hot electron thermalization. **TODO: figure**

The hot electrons described by the two-temperature model emit thermal radiation during their cooling process. The spectral energy density of this radiation follows Planck's law:

$$B(\lambda, T) = \frac{2hc^2}{\lambda^5} \frac{1}{\exp\left(\frac{hc}{\lambda kT}\right) - 1} \quad (2)$$

where  $h$  is Planck's constant,  $c$  is the speed of light,  $k$  is the Boltzmann constant, and  $T$  is the electron temperature. Since hot electron temperatures reach values of several thousand Kelvin and far exceed lattice temperatures during femtosecond excitation, the thermal radiation spectrum of hot electrons dominates over that of the lattice. For the time-dependent electron temperature  $T_e(t)$  predicted by the two-temperature model, the total thermal radiation spectrum is obtained by integrating Planck's law over the entire cooling dynamics. **TODO: figure showing simulated thermal radiation spectrum**

The theoretical predictions from the two-temperature model indicate that thermal radiation from hot electrons should produce a low power, broadband spectrum spanning the visible and near-infrared regions. Building upon this understanding, Roob conceptualized a experimental setup to measure the thermal radiation of the hot electrons [5]. The ultrafast hot electrons are characterized by their emitted thermal radiation, utilizing graphite as the sample material due to its well-characterized electronic properties [6] and easy procurement.

The present internship work focuses on the optimization and calibration of the experimental setup developed by Roob [5]. The primary objective was to improve the measurement of thermal emissions from ultrafast hot electrons through systematic characterization of noise sources in EMCCD detection systems [8, 9] and calibration of the quantum efficiency of the spectrometer system. This report presents the experimental setup optimization, noise analysis, and theoretical framework for spectrometer calibration.

## 2 Experimental Setup

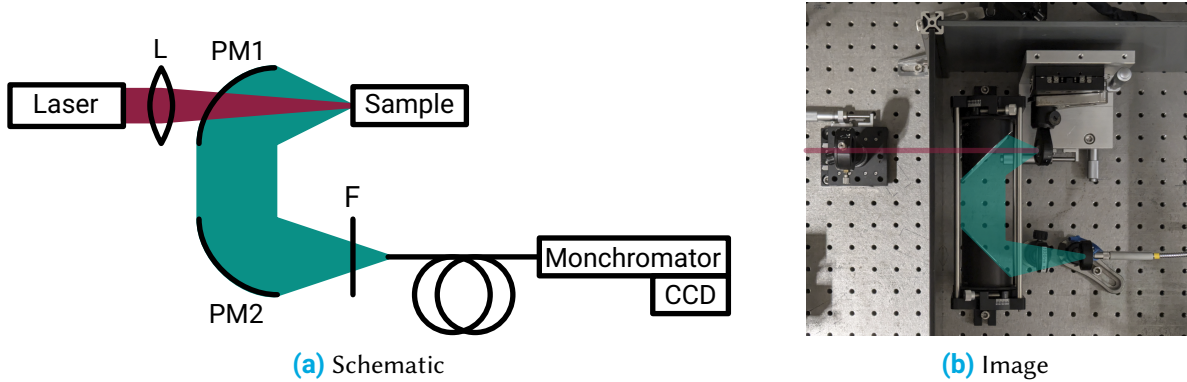


**Figure 1** Experimental Setup.

The experimental setup, designed by Leon Roob [5], is shown schematically in Figure ???. This broadband photoemission configuration enables measurement of thermal emission from ultrafast hot electrons.

The excitation source is a Pharos PH1-20 laser (Light Conversion) operating at 1030 nm wavelength with 250 fs FWHM pulse duration and 100 kHz repetition rate. The beam undergoes 4-axis stabilization and is expanded to a diameter of 5 mm upon entering the experimental chamber. A focusing lens (L) with 200 mm focal length creates a diffraction-limited spot size of  $4\lambda f/\pi D = 50 \mu\text{m}$  on the sample surface.

Upon laser excitation, the sample absorbs the pulse energy and emits thermal radiation into the collection hemisphere. The broadband emission is collected using UV-enhanced aluminum-coated off-axis parabolic mirrors (PM). Mirror PM1 (50 mm focal length) collects the emission, while PM2 (101 mm focal length) focuses the light through a spectral filter onto a bare multimode fiber end. This mirror configuration provides a magnification of  $f_{\text{PM2}}/f_{\text{PM1}} = 2$  for the collected thermal emission. Therefore the spotsize is roughly 100  $\mu\text{m}$  in diameter.

The optical fiber (QP200-2-SR-BX, Ocean Optics) is a 200  $\mu\text{m}$  core multimode fiber optimized for 300–1100 nm transmission. Spectral analysis employs an Acton SpectraPro 300i monochromator equipped with a 150 lines/mm grating blazed at 500 nm. Detection utilizes an Andor iXon<sup>EM+</sup> 897 EMCCD camera operated in vertical binning mode as a line detector.

For alignment optimization, lens L, the sample, and fiber end are mounted on 3-axis translation stages, while the parabolic mirrors remain fixed.

## 3 Characterization of Noise Sources

Detecting the weak thermal radiation from hot electrons requires careful optimization of the signal-to-noise ratio (SNR). The dominant noise sources originate from the detector, while laser power fluctuations are assumed negligible.

The EMCCD detector exhibits several characteristic noise mechanisms well-documented by Andor [8, 9] and detailed in [10].

**Readout noise** represents the fundamental noise floor, arising from charge transfer operations and analog-to-digital conversion. For this high-performance CCD, readout noise measures approximately 1 e<sup>-</sup> [11], consistent with measurements shown in Figure 2. Since this noise applies per readout bin rather than per pixel, hardware vertical binning effectively reduces its impact.

**Dark current noise** results from thermal excitation of electrons within the detector semiconductor,

following the relationship  $N_{\text{dark}} \propto \exp(-E/kT) \cdot t_{\text{exp}}$ , as demonstrated in [Figure 2](#). Cooling the detector to  $-80^{\circ}\text{C}$  effectively suppresses this contribution, rendering it negligible for typical exposure times.

**Clock-induced charge noise** scales with electron multiplication gain and signal amplitude. Therefore, sensor gain is deactivated when signal levels significantly exceed readout noise [8], as in the present configuration.

Under these optimized conditions, **shot noise** becomes the dominant limitation, establishing shot noise-limited operation as shown in [Figure 3](#). **TODO**

## 4 Efficiency and Flatness

The detection efficiency—defined as the fraction of sample-emitted light reaching the detector—varies with wavelength due to component-specific spectral responses.

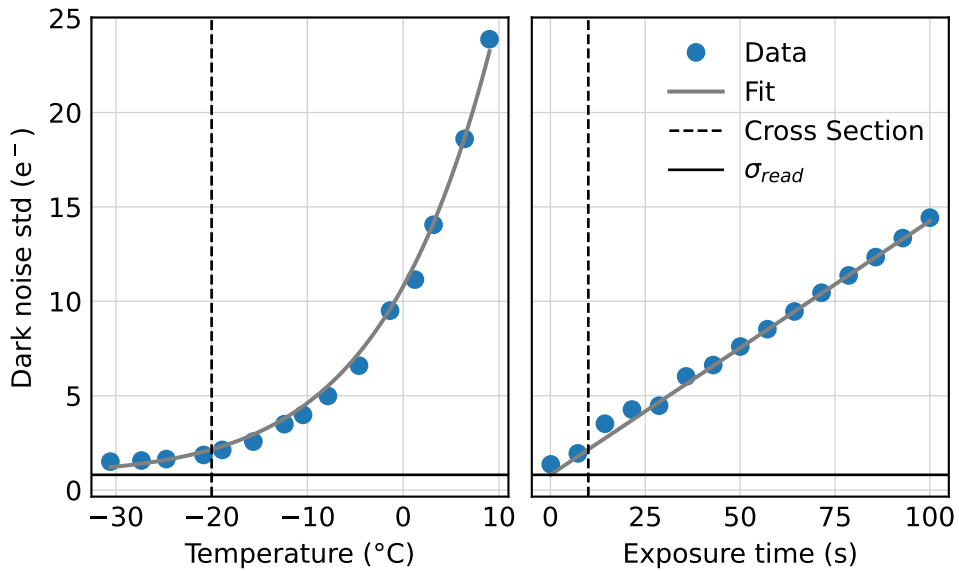


**Figure 2** Dark noise as a function of sensor temperature and exposure time. The fitted curve yields an effective activation energy of  $E = 0.597(4)\text{ eV}$  and constant readout noise of  $\sigma_{\text{read}} = 0.81(12)\text{ e}^-$ .

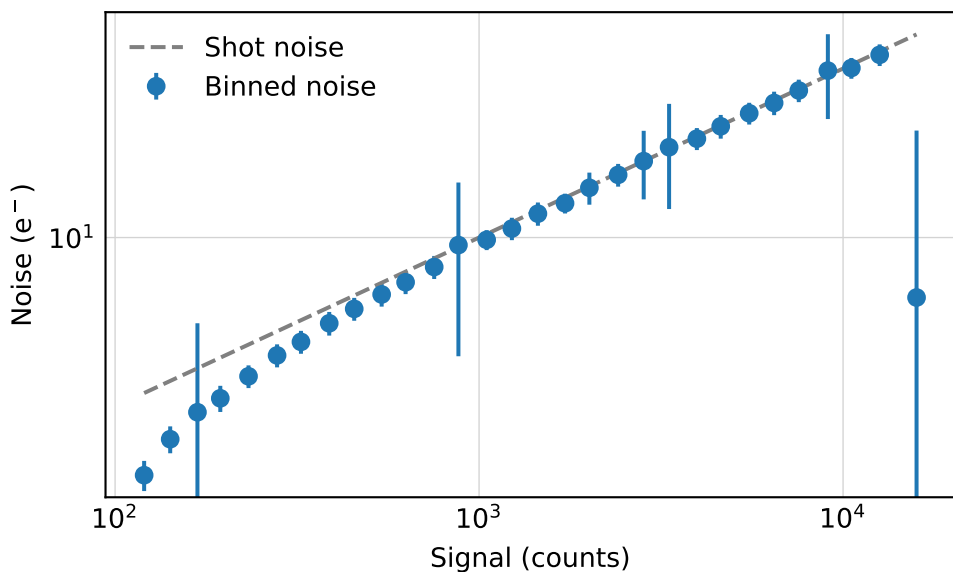


**Figure 3** Measured noise versus signal, demonstrating shot noise-limited performance.

The parabolic mirrors and optical fiber exhibit relatively flat spectral responses across the detection range, contributing primarily constant efficiency factors. However, other components introduce wavelength-dependent losses that must be characterized.

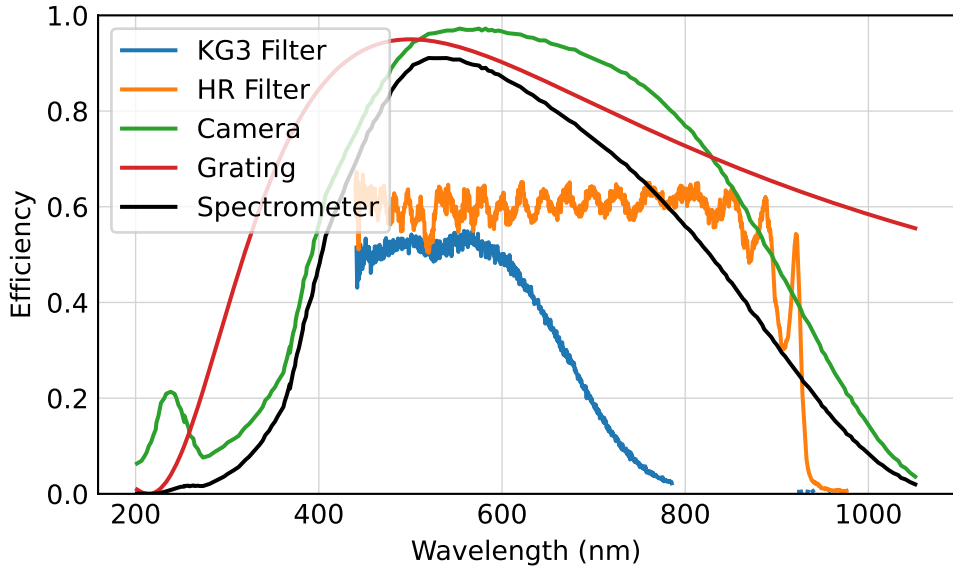


**Figure 4** Spectral efficiency of various optical components and filters employed in the setup.

Spectral filters for laser rejection exhibit distinct transmission characteristics, as shown in Figure 4. The SCHOTT KG3 filter, designed for infrared absorption, displays a gradual transmission edge that attenuates expected thermal emission. The HR filter, identified as a dielectric shortpass filter (likely Edmund Optics), shows sharper cutoff behavior, though detailed specifications were unavailable.

The detector quantum efficiency and grating efficiency curves require more sophisticated characterization. Figure 4 presents the manufacturer-specified quantum efficiency for the EMCCD camera. Grating efficiency calculations employ the blazed grating model from [12], accounting for wavelength-dependent diffraction characteristics.

#### 4.1 Calibration

Spectrometer efficiency calibration requires a reference source with precisely known spectral characteristics. The standard approach employs calibrated white light sources with traceable spectral irradiance standards.

An alternative calibration approach was attempted using multiple uncalibrated Ocean Optics USB spectrometers to characterize a deuterium-halogen lamp (DH-2000-BAL, Ocean Optics). Figure 5 presents the resulting spectra, with intensity scaling adjusted for different instrument sensitivities. The significant disagreement between instruments highlights the necessity for calibration against more reliable reference standards.

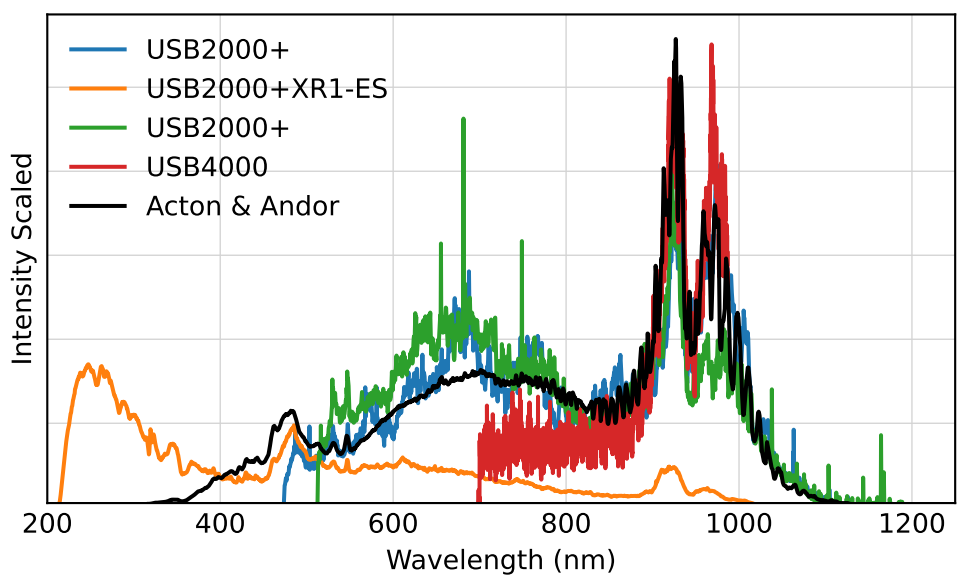


**Figure 5** Identical spectrum recorded with different spectrometer systems, illustrating calibration discrepancies.

## 5 Data Analysis and Spectral Modeling

## 6 Conclusion

## References

- [1] Chun Hung Lui, Kin Fai Mak, Jie Shan, and Tony F. Heinz. "Ultrafast Photoluminescence from Graphene". In: *Physical Review Letters* 105.12 (Sept. 2010). Publisher: American Physical Society, p. 127404. doi: [10.1103/PhysRevLett.105.127404](https://doi.org/10.1103/PhysRevLett.105.127404). URL: <https://link.aps.org/doi/10.1103/PhysRevLett.105.127404> (visited on 05/05/2025).
- [2] A. Stange, C. Sohrt, L. X. Yang, G. Rohde, K. Janssen, P. Hein, L.-P. Oloff, K. Hanff, K. Rossnagel, and M. Bauer. "Hot electron cooling in graphite: Supercollision versus hot phonon decay". In: *Physical Review B* 92.18 (Nov. 2015). Publisher: American Physical Society, p. 184303. doi: [10.1103/PhysRevB.92.184303](https://doi.org/10.1103/PhysRevB.92.184303). URL: <https://link.aps.org/doi/10.1103/PhysRevB.92.184303> (visited on 04/01/2025).
- [3] Haibin Tang, Chih-Jung Chen, Zhulin Huang, Joeseph Bright, Guowen Meng, Ru-Shi Liu, and Nianqiang Wu. "Plasmonic hot electrons for sensing, photodetection, and solar energy applications: A perspective". In: *The Journal of Chemical Physics* 152.22 (June 2020), p. 220901. ISSN: 0021-9606. doi: [10.1063/5.0005334](https://doi.org/10.1063/5.0005334). URL: <https://doi.org/10.1063/5.0005334> (visited on 07/24/2025).
- [4] D. König, K. Casalenuovo, Y. Takeda, G. Conibeer, J. F. Guillemoles, R. Patterson, L. M. Huang, and M. A. Green. "Hot carrier solar cells: Principles, materials and design". In: *Physica E: Low-dimensional Systems and Nanostructures*. 14th International Conference on Modulated Semiconductor Structures 42.10 (Sept. 2010), pp. 2862–2866. ISSN: 1386-9477. doi: [10.1016/j.physe.2009.12.032](https://doi.org/10.1016/j.physe.2009.12.032). URL: <https://www.sciencedirect.com/science/article/pii/S138694770900650X> (visited on 07/24/2025).
- [5] Leon Roob. "Thermal Radiation from Ultrafast Hot Electrons in Graphite". en. Universität Konstanz, Apr. 2025.
- [6] Takeshi Nihira and Tadao Iwata. "Temperature dependence of lattice vibrations and analysis of the specific heat of graphite". In: *Physical Review B* 68.13 (Oct. 2003). Publisher: American Physical Society, p. 134305. doi: [10.1103/PhysRevB.68.134305](https://doi.org/10.1103/PhysRevB.68.134305). URL: <https://link.aps.org/doi/10.1103/PhysRevB.68.134305> (visited on 04/01/2025).
- [7] Tobias Kampfrath, Luca Perfetti, Florian Schapper, Christian Frischkorn, and Martin Wolf. "Strongly Coupled Optical Phonons in the Ultrafast Dynamics of the Electronic Energy and Current Relaxation in Graphite". en. In: *Physical Review Letters* 95.18 (Oct. 2005), p. 187403. ISSN: 0031-9007, 1079-7114. doi: [10.1103/PhysRevLett.95.187403](https://doi.org/10.1103/PhysRevLett.95.187403). URL: <https://link.aps.org/doi/10.1103/PhysRevLett.95.187403> (visited on 05/13/2025).
- [8] Andor. *Establishing Sensitivity in Scientific Cameras*.
- [9] Dr. Jo Walters. *Sensitivity and Noise of CCD, EMCCD and sCMOS Sensors*. Apr. 2023.
- [10] European Machine Vision Association. *Standard for Characterization of Image Sensors and Cameras*. Nov. 2010.
- [11] Andor. *iXonEM+ 897*.
- [12] P. K. Barker. "Ripple correction of high-dispersion IUE spectra - Blazing echelles". en. In: *The Astronomical Journal* 89 (June 1984), p. 899. ISSN: 00046256. doi: [10.1086/113587](https://doi.org/10.1086/113587). URL: [http://adsabs.harvard.edu/cgi-bin/bib\\_query?1984AJ.....89..899B](http://adsabs.harvard.edu/cgi-bin/bib_query?1984AJ.....89..899B) (visited on 04/07/2025).